Lanthanide-Based Heteroepitaxial Core–Shell Nanostructures: Compressive *versus* Tensile Strain Asymmetry

Noah J. J. Johnson and Frank C. J. M. van Veggel*

Department of Chemistry, University of Victoria, Victoria, BC V8W 3V6, Canada

ABSTRACT Heteroepitaxial core–shell nanostructures have been proven advantageous in a wide variety of applications, ranging from luminescence enhancement, band gap engineering, multimodal theranostics, to catalysis. However, precisely tailoring the epitaxial growth is challenging, and a general understanding of the parameters that impact epitaxial growth remains unclear. Here we demonstrate the critical role of the sign of the lattice mismatch of the shell relative to the core (compressed/tensile) in generating lanthanide-based core–shell structures, a parameter conventionally not considered in heteroepitaxial design. We took advantage of the very gradual contraction of lanthanide ions along the series to control precisely both the magnitude and the sign of lattice mismatch and investigated multiple sodium lanthanide fluoride ($NaLnF_4$) core–shell heterostructures of variable composition and size. We discovered that the tensile strained shells adapt to the core crystallite shape (*i.e.*, conformal) and lattice structure (*i.e.*, coherent), while under identical magnitude of mismatch, the compressively strained shells are neither conformal nor coherent to the core. This striking asymmetry between the tensile and compressively strained epitaxial growth arises from the fundamental anharmonicity of the interatomic interactions between the attractive and repulsive pairs. From a broader perspective, our findings redefine the *a priori* design consideration and provide a fundamental insight on the necessity to include the sign of lattice mismatch and not just its magnitude in designing heteroepitaxial core–shell nanostructures.

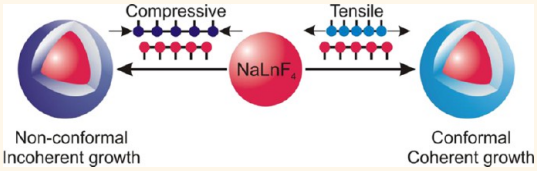

KEYWORDS: lanthanides · core–shell · epitaxy · heterostructures · lattice mismatch · growth mechanism

In epitaxial growth of lattice mismatched materials, the shell lattice adapts to the underlying core lattice structure, resulting in substantial lattice strain in the epitaxial layer (shell). The strain in the epitaxial layer beyond a critical thickness (about 1–2 monolayers; MLs) relaxes, leading to shape inhomogeneity and anisotropic structures.[1,2] Critical for growing thick shells, it is generally accepted that the lattice mismatch between the core and the shell should be minimal (<2%), and conventionally, core–shell structures are designed based on this minimal mismatch consideration.[3] However, epitaxial shell growth in lanthanide-based nanostructures, despite their chemical similarity and minimal lattice mismatch, often results in anisotropic growth as opposed to the highly desired isotropic/centrosymmetric growth.[4–6] Given the wide ranging possibilities to generate distinctive properties through epitaxial shell growth in this class of nanomaterials,[7–10] new insights for designing isotropic core–shell structures are needed.

In epitaxial growth as the shell lattice adapts to the core lattice structure, the shell lattice compresses when it is larger than the core (negative mismatch) and expands when it is smaller (positive mismatch). Fundamentally, the interaction potentials of atoms/ions, the basic building blocks of materials, are anharmonic between the attractive and repulsive pairs (*e.g.*, Lennard-Jones 6–12 potential), and therefore, the sign of mismatch is expected to influence directly the core–shell epitaxial growth. However, the sign of lattice mismatch of the shell relative to the core is generally disregarded, and its impact on the core–shell structures thus remains poorly understood. Elements in the lanthanide series have similar chemical properties, while their ionic radii decrease gradually with increase in atomic number from lanthanum (La^{3+}, r = 1.300 Å) to lutetium (Lu^{3+},

* Address correspondence to fvv@uvic.ca.

Received for review July 17, 2014 and accepted October 7, 2014.

Published online October 07, 2014
10.1021/nn503946t

r = 1.117 Å), referred to as the lanthanide contraction. This unique property of the lanthanides provides a highly flexible template to investigate heteroepitaxial core−shell growth under multiple parameters such as magnitude of lattice mismatch strain, sign of lattice mismatch, crystallite size, and variable core−shell compositions with identical crystal phase. We chose hexagonal phase (β) $NaLnF_4$ nanostructures, one of the well-studied lanthanide-based materials to date,[11−14] as a model system. The decrease in ionic radii along the lanthanide series results in a gradual decrease of the crystal lattice parameters (Supporting Information Table S1), and this allows for precise manipulation of both the magnitude and sign of lattice mismatch, simply by varying the core and shell composition.

RESULTS AND DISCUSSION

Hexagonal phase (β) $NaYF_4$, $NaErF_4$, and $NaDyF_4$ with different crystallite sizes (~20, 15, and 10 nm, respectively) were used as core nanocrystals (Figure 1), allowing the investigation of the effect of core size and composition in epitaxial growth. The core nanocrystals were of high crystal phase purity, as confirmed by powder X-ray diffraction (XRD) analysis (Supporting Information Figure S1). The size distribution analyses from the transmission electron microscopy (TEM) images and the XRD patterns are in good agreement, confirming the narrow size dispersion of the synthesized core nanocrystals (Figure 1 and Supporting Information Figure S2). The epitaxial shell growth on the core nanocrystals was performed by hot-injection of smaller kinetic phase (α cubic) sacrificial nanocrystals as shell precursors directly into the core reaction mixture (see Materials and Methods section for details), resulting in epitaxial shell deposition by Ostwald ripening mediated "self-focusing".[15] Driven by Ostwald ripening, the energetically less favored sacrificial nanocrystals rapidly dissolve and deposit as hexagonal

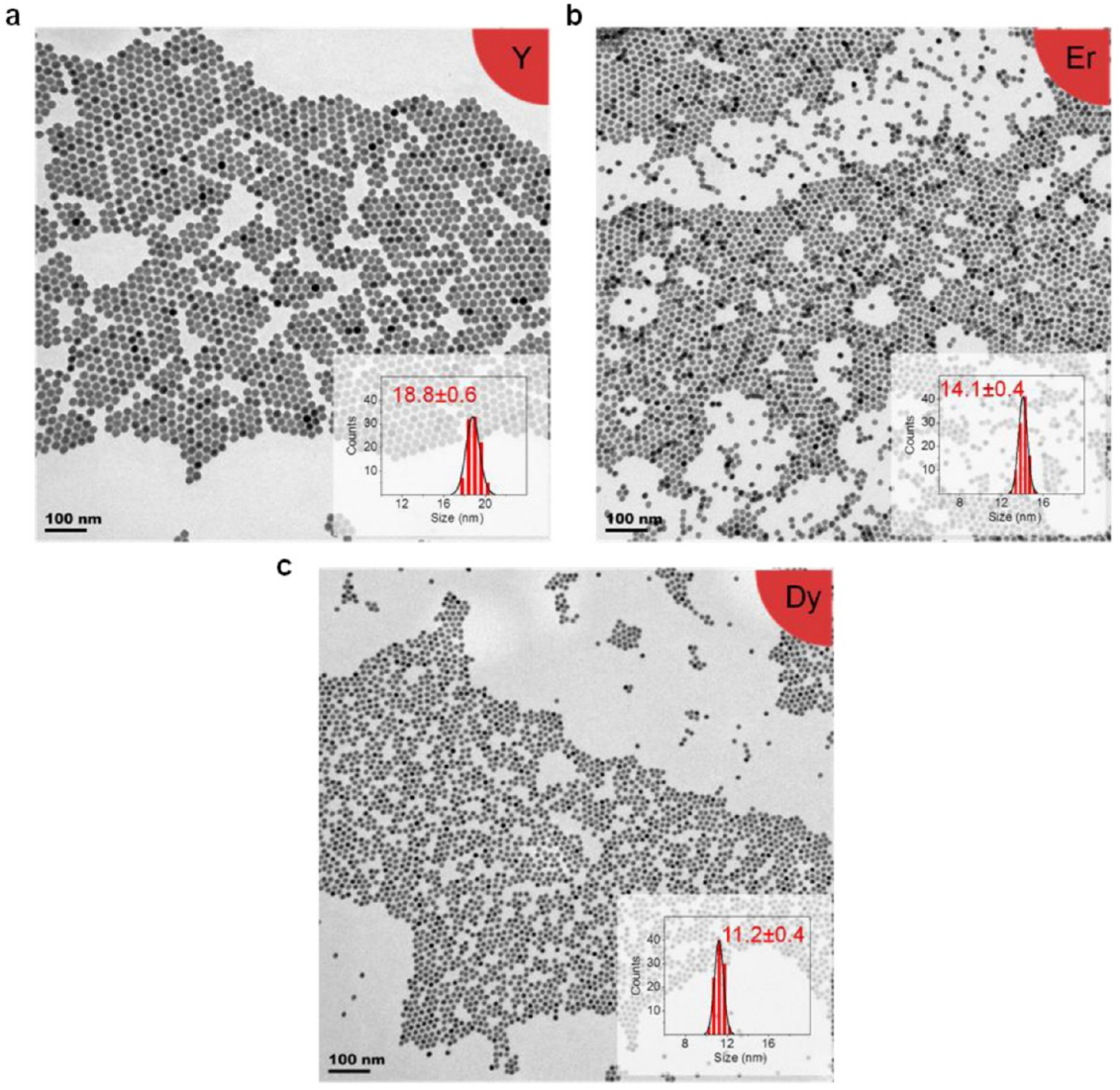

Figure 1. TEM images of core nanocrystals: (a) $NaYF_4$, (b) $NaErF_4$, and (c) $NaDyF_4$. Size distribution of the core nanocrystals (inset). The labels Y, Er, and Dy refer to $NaYF_4$, $NaErF_4$, and $NaDyF_4$ respectively.

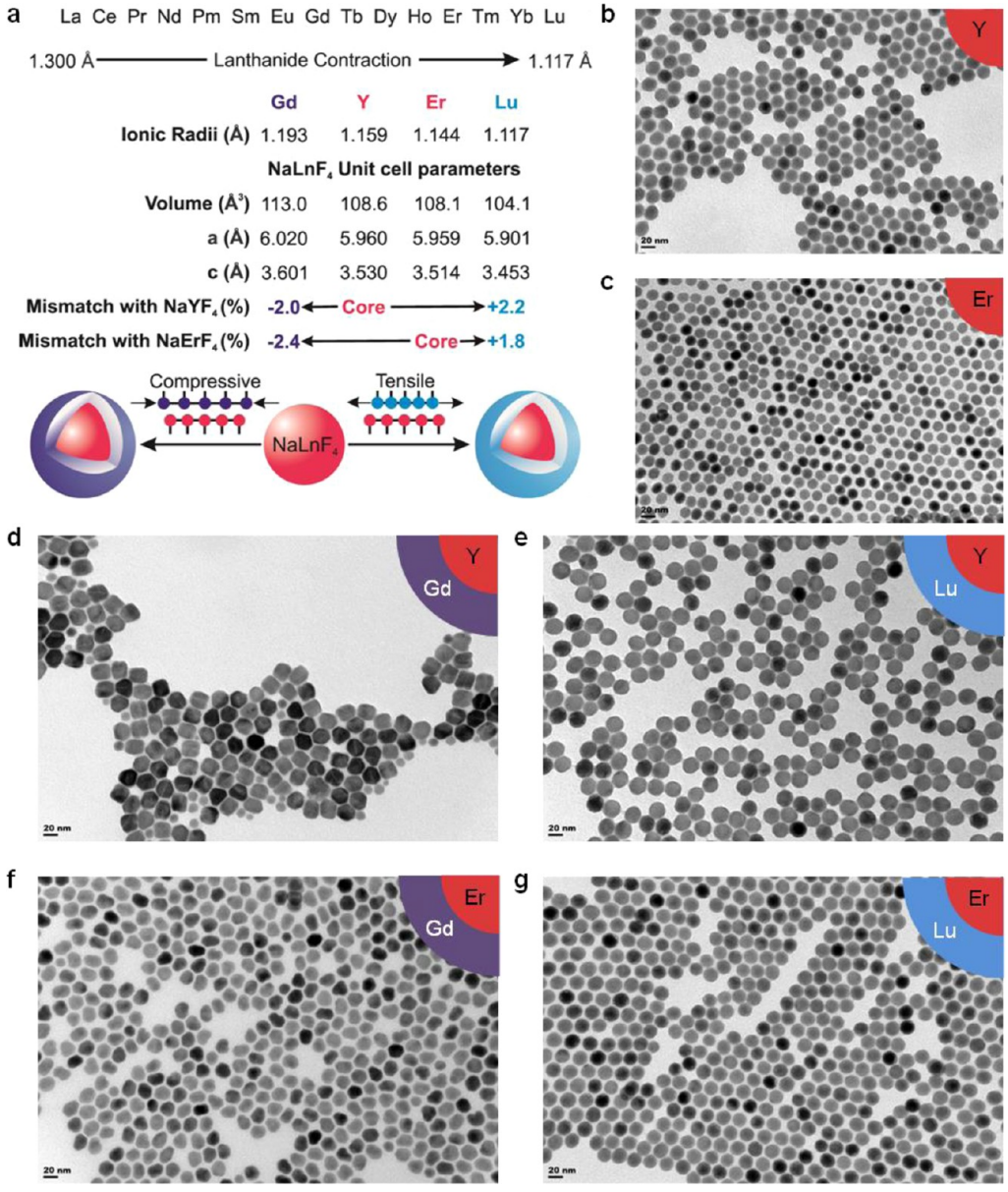

Figure 2. Compressive and tensile strained epitaxial core–shell nanocrystals. (a) Lanthanide (Ln^{3+}) contraction and lattice parameters of hexagonal phase $NaGdF_4$, $NaYF_4$, $NaErF_4$, and $NaLuF_4$, demonstrating the flexibility in manipulating structural composition, magnitude, and sign of lattice mismatch simultaneously. (b,c) Representative TEM images of core $NaYF_4$ (18.8 ± 0.6 nm) and $NaErF_4$ (14.1 ± 0.4 nm) nanocrystals, respectively, showing uniform quasi-spherical shape and narrow size dispersity. TEM images of core–shell nanocrystals: (d) $NaYF_4$–$NaGdF_4$, (e) $NaYF_4$–$NaLuF_4$, (f) $NaErF_4$–$NaGdF_4$, and (g) $NaErF_4$–$NaLuF_4$. Scale bar = 20 nm in all TEM images. The core–shell structures with a tensile strained shell maintain the quasi-spherical shape of the core nanocrystals (e,g), demonstrating a conformal growth, while the compressively strained shell result in anisotropic structures (d,f). The lattice mismatch between the core and the shell is determined based on shorter axis using the formula $f = (c_{core} - c_{shell})/c_{shell}$, when $c_{shell} > c_{core} \rightarrow f < 0$ (negative mismatch, compressively strained) and $c_{shell} < c_{core} \rightarrow f > 0$ (positive mismatch, tensile strain).

epitaxial layers on the core nanocrystals. We have previously demonstrated the high degree of control offered by this method to grow epitaxial layers tunable both in thickness and in composition in this class of nanostructures.[15] Moreover, the isotropic quasi-spherical nature of the core nanocrystals employed in this work allows us to study the impact of epitaxial growth on the structural evolution of the core–shell nanocrystals and compare it with classical growth modes known in thin film epitaxy on single crystal substrates.

Considering only the magnitude of lattice mismatch between the core and the epitaxial layer, the epitaxial growth of $NaGdF_4$ or $NaLuF_4$ on a $NaYF_4$ core is expected to be the same, given their identical magnitude of lattice mismatch (~2%) with respect to the core (Figure 2a). However, the TEM images clearly show different growth modes (Figure 2d,e). The compressed $NaGdF_4$ shell growth (negative mismatch) results in highly anisotropic structures (Figure 2d), while the tensile $NaLuF_4$ shell growth (positive mismatch)

remains isotropic (Figure 2e). Interestingly, the shape of the tensile $NaYF_4$–$NaLuF_4$ core–shell structure is identical to the core (quasi-spherical) with an average size increase from 18.3 ± 0.4 to 24.3 ± 0.7 nm, indicating a uniform conformal shell growth of 3 nm in thickness (~9 MLs), in contrast to the $NaYF_4$–$NaGdF_4$ core-compressed shell which forms anisotropic structures (Supporting Information Figure S3). To confirm this remarkably different epitaxial growth with reversal in the sign of lattice mismatch, we examined the epitaxial growth of the same shell materials $NaGdF_4$ and $NaLuF_4$ on a different core composition using 14 nm $NaErF_4$ nanocrystals (Figures 1b and 2c) as a core. The change in composition and size of the core did not influence the nature of the epitaxial growth, and the core–shell structures are once again strikingly dissimilar based on the sign of the mismatch (Figure 2f,g and Supporting Information Figure S4). In addition, the core–shell structures with a tensile shell form well-packed hexagonal arrays on the TEM grid, as expected for quasi-spherical particles (hard spheres) with a low size dispersion, while the compressed shell ones, which are anisotropic, hardly yield long-range ordering, as demonstrated in the low-resolution TEM images (Supporting Information Figures S5 and S6). This further corroborates the difference in the core–shell morphology with reversal in the sign of lattice mismatch. To provide further evidence, we extended our study to 11 nm $NaDyF_4$ core nanocrystals (Figure 1c), on which two different compositions of tensile ($NaDyF_4$–$NaTmF_4$ and $NaDyF_4$–$NaYbF_4$) and compressed ($NaDyF_4$–$NaEuF_4$ and $NaDyF_4$–$NaSmF_4$) epitaxial shells were grown (Supporting Information Figure S7). Here, too, we observe only the core–shell structures with a tensile shell to be conformal (Figure 3 and Supporting Information Figures S8–S10), which further supports our findings and demonstrates the effect of the sign of mismatch in generating conformal and nonconformal structures. To highlight, the lattice mismatch between the compressed $NaDyF_4$–$NaSmF_4$ and tensile $NaDyF_4$–$NaYbF_4$ is almost identical at ~2.4%, and the structural difference in the core–shell morphology shown in Figure 3 demonstrates the effect of the sign of mismatch in heteroepitaxial growth.

The observed influence of the sign of mismatch in epitaxial growth arises from the anharmonicity of the interatomic interaction potentials between the attractive (tensile) and repulsive (compression) pairs. As the interaction potential is highly asymmetric, the sign of the mismatch is expected to influence the epitaxial growth even when the magnitude of lattice mismatch is less than 2% (conventionally considered favorable for conformal epitaxial growth). In order to validate this, we used $NaYF_4$ as the core to grow two different sets of compressed and tensile epitaxial shells of moderate lattice mismatch (<2%; see Supporting Information Figure S11) as compared to previously discussed $NaGdF_4$ and $NaLuF_4$ shell (~2%) (Figure 2a). The TEM images of the core–shell structures are compared with the respective core in Figure 4 (compressed shell) and Figure 5 (tensile shell), where it can be seen that only the tensile shells conform to the shape of the core while the compressed shells are anisotropic, irrespective of the magnitude of the lattice mismatch. Especially, in the case of compressed shells, the anisotropy of the core–shell structures is clearly evident as increased faceting even under very minimal lattice mismatch as observed for the $NaYF_4$–$NaDyF_4$ (−0.7%) (Figure 4a). On the other hand, the tensile strained epitaxial growth results in quasi-spherical structures (Figure 5).

To study further, we used the large difference in the atomic number of yttrium (Z = 39) relative to the lanthanide composition in the shell (Z = 64 for Gd and Z = 71 for Lu) to obtain Z-contrast high-angle annular dark-field (HAADF) images.[4] The HAADF images show clear contrast between the core (dark) and shell (bright), confirming the shell growth (Figure 6). The HAADF images also show that the anisotropy increases with increasing lattice mismatch for the core–shell structures with compressed shell (Figure 6a–c while all tensile core–shell structures are conformal (Figure 6d–f). The high-resolution (HR)-HAADF images for the core–shell structures with compressed shell shown in Figure 7a–c and Supporting Information Figures S12–S14 more clearly show the increasing anisotropy with increasing lattice mismatch. Interestingly, the stability of the core–shell structures under the electron beam was different for the compressed and tensile core–shell structures. The tensile conformal core–shell structures were unstable under the high-energy electron beam during HR-HAADF imaging and underwent rapid beam damage (Figure 7d–f and Supporting Information Figures S15–S17), in contrast to images obtained at low-resolution (Supporting Information Figures S18–S20). Moreover, these structures underwent beam damage even under cryo conditions and conventional TEM imaging (Supporting Information Figures S21 and S22). The initial beam damage on exposure to the electron beam shows circular patterns on the TEM images (Supporting Information Figure S22), suggesting that it occurs at the core and shell interface. This stark contrast in sample stability under the electron beam indicates that the conformal core–shell structures are strained, while the nonconformal core–shell structures are strain relaxed. To study this structural difference, we performed XRD analysis on the core–shell nanocrystals.

Along the lanthanide series, as the unit cell contracts with increasing atomic number, the XRD peaks of hexagonal phase $NaLnF_4$ shift to higher diffraction angles (2θ) (Supporting Information Figure S23), a useful feature that allowed us to analyze systematically the XRD patterns of the core–shell nanocrystals.

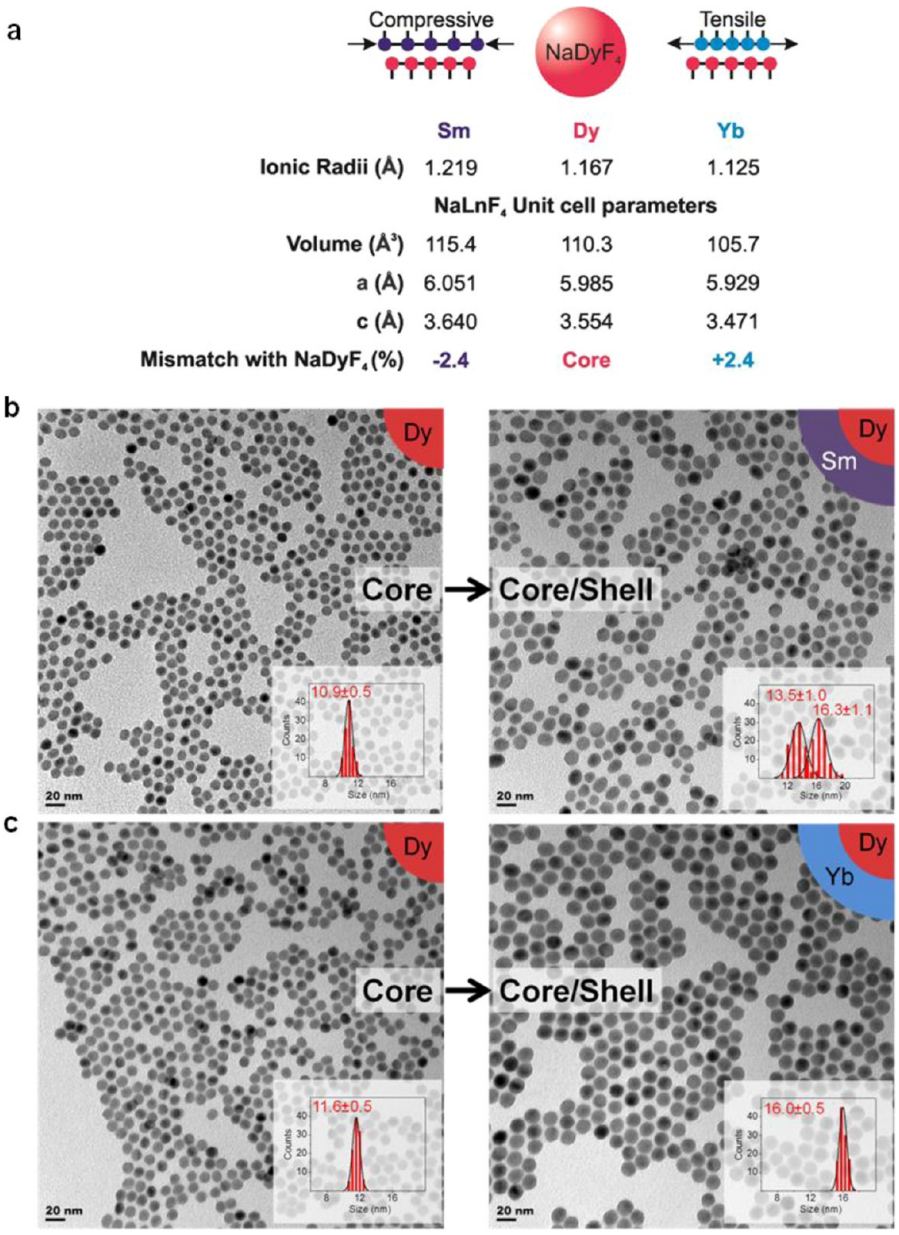

Figure 3. Compressive and tensile strained epitaxial core−shell nanocrystals with almost identical magnitude of lattice mismatch between the core and the shell. (a) Lattice parameters of hexagonal phase $NaDyF_4$, $NaSmF_4$, and $NaYbF_4$. TEM images of (b) $NaDyF_4$ core (left), $NaDyF_4$−$NaSmF_4$ core-compressed shell (right), and (c) $NaDyF_4$ core (left), $NaDyF_4$−$NaYbF_4$ core-tensile shell (right) nanocrystals. Scale bar = 20 nm in all TEM images. Size distribution of the core and core−shell nanocrystals (inset).

In epitaxial growth, as the shell lattice adapts to the core lattice, the XRD pattern of the resulting core−shell structure is expected to match with the core diffraction pattern if the epitaxial layer remains coherent to the core. Apparently, all the XRD patterns of the core−shell structures with compressed shell are shifted toward lower diffraction angles with respect to the core, irrespective of the magnitude of the lattice mismatch (Figure 8a and Supporting Information Figure S24). Thus, the compressed shells are incoherent to the core, in addition to their shapes being nonconformal (Figures 6a−c and 7a−c). In contrast, the XRD patterns for all of the conformal tensile core−shell structures match with the core lattice pattern (Figure 8b and Supporting Information Figure S25), confirming a coherent epitaxial growth. This is remarkable considering the fact that all core−shell compositions described here contain more of the shell material relative to the core (see Materials and Methods section for details). We also confirmed this structural difference for all of the other core−shell structures synthesized and found only the tensile strained shells to be coherent to the core (Supporting Information Figures S26−S28).

The results described thus far demonstrate the significance of the sign of the mismatch in the epitaxial growth of lattice mismatched heterostructures.

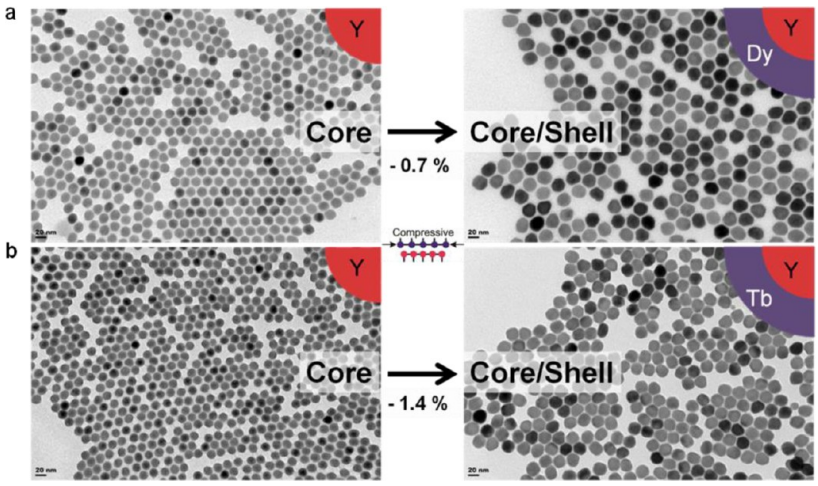

Figure 4. TEM images of core and core−shell nanocrystals with compressed shell and lattice mismatch less than 2%. (a) $NaYF_4$ core (left) and $NaYF_4$−$NaDyF_4$ core−shell (−0.7%) (right), and (b) $NaYF_4$ core (left) and and $NaYF_4$−$NaTbF_4$ core−shell (−1.4%) (right). Scale bar = 20 nm in all TEM images.

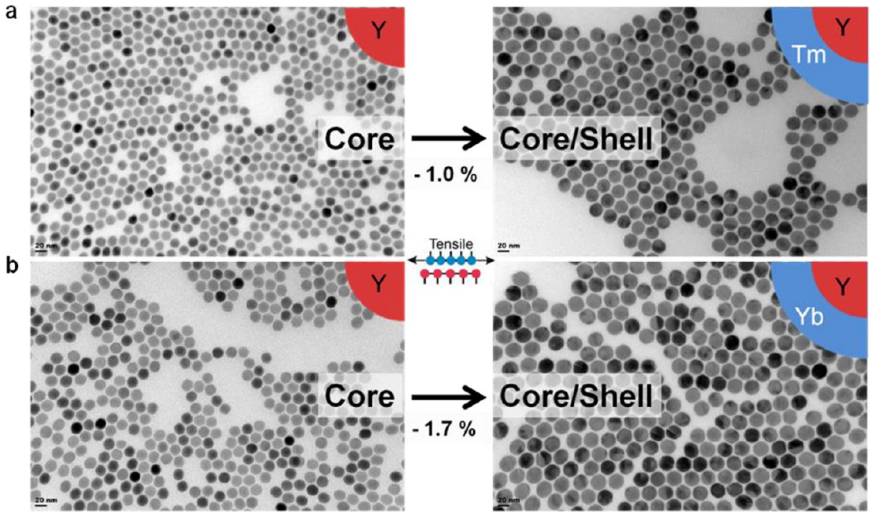

Figure 5. TEM images of core and core−shell nanocrystals with tensile shell and lattice mismatch less than 2%. (a) $NaYF_4$ core (left) and $NaYF_4$−$NaTmF_4$ core−shell (−1.0%) (right), and (b) $NaYF_4$ core (left) and $NaYF_4$−$NaYbF_4$ core−shell (−1.7%) (right). Scale bar = 20 nm in all TEM images.

We now focus on the structural evolution of the core−shell nanocrystals and compare the compressed and tensile epitaxial growth with classical growth modes of thin film epitaxy (Figure 8c).[16] During shell growth, the compressively strained shell, after a few MLs, undergoes strain relaxation by surface diffusion of adatoms from high-energy to low-energy facets, similar to the Stranski-Krastanov (SK) layer-island growth mode. This surface diffusion of adatoms results in surface roughening (nonconformal structures), and the strain relaxation of the epitaxial layer leads to incoherent structures, as confirmed by the XRD patterns (Figure 8a). Moreover, the strain relaxation of the epitaxial layer during compressively strained shell growth leads to reaction-limited growth with increasing lattice mismatch, as observed by the increase in structural anisotropy with increasing mismatch and the presence of small nanocrystals in the case of core−shell structures with relatively large negative mismatch (Figure 2d,f and Figure 3b). Note that we deposit the epitaxial layers by ripening using sacrificial nanocrystals, and when the shell growth becomes reaction-limited, the ripening competes with the redistribution of shell material from high-energy to low-energy facets. Thus, in the case of the compressively strained shell growth, with an increase in the magnitude of lattice mismatch between the core and the shell, the structures become more anisotropic (Figure 2d and Figure 4). In the case of $NaYF_4$−$NaGdF_4$, we have previously demonstrated uniform thin shell growth of about ~2−3 MLs without strain relaxation.[15] However, with an increase in shell thickness, the compressive strain in the epitaxial layer caused by the negative mismatch leads to strain relaxation,

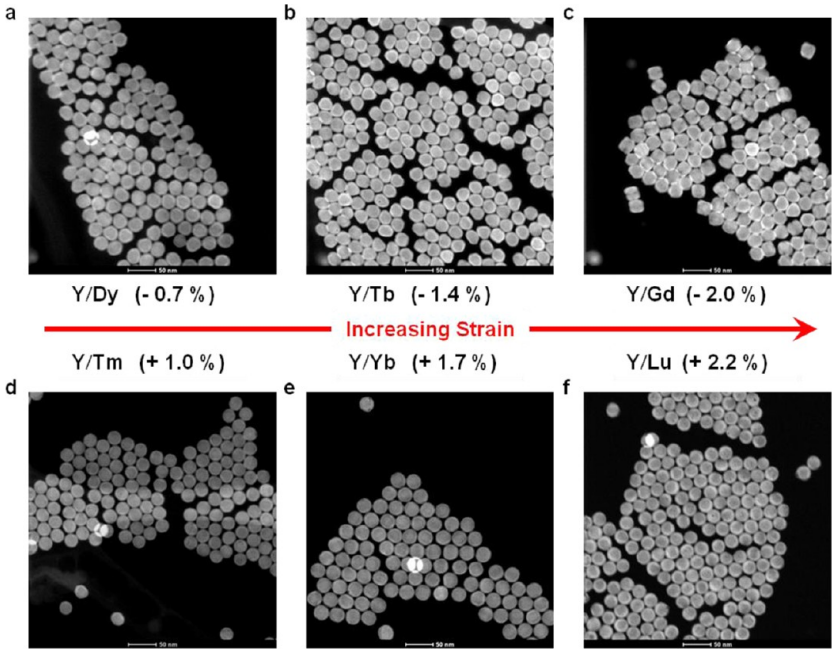

Figure 6. HAADF (*Z*-contrast) images of core–shell nanocrystals: (a) $NaYF_4$–$NaDyF_4$, (b) $NaYF_4$–$NaTbF_4$, (c) $NaYF_4$–$NaGdF_4$, (d) $NaYF_4$–$NaTmF_4$, (e) $NaYF_4$–$NaYbF_4$, and (f) $NaYF_4$–$NaLuF_4$. Scale bar = 50 nm in all HAADF images. The shell appears bright relative to the core, resulting from the large difference in the atomic number of yttrium (Z = 39) in the core relative to the lanthanide composition in the shell (Z = 64 for Gd and Z = 71 for Lu).

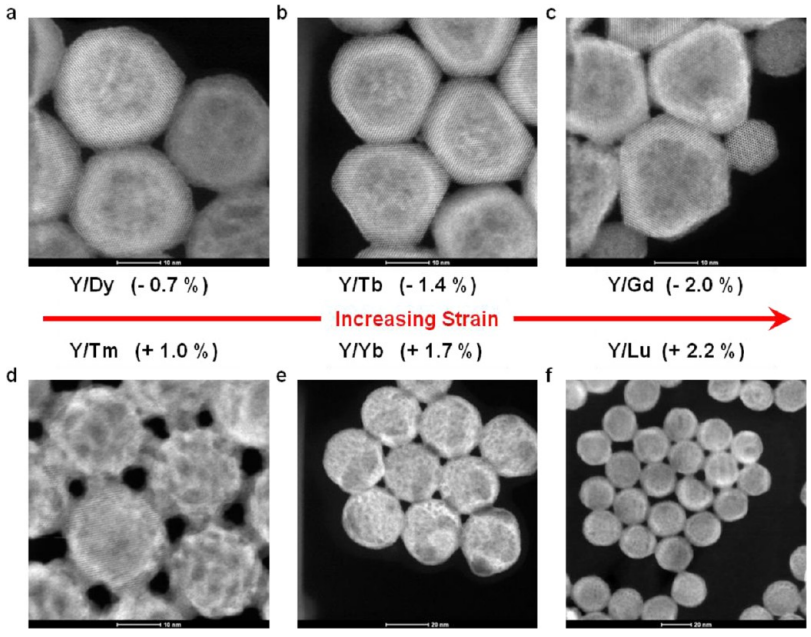

Figure 7. High-resolution HAADF images of core–shell nanocrystals: (a) $NaYF_4$–$NaDyF_4$, (b) $NaYF_4$–$NaTbF_4$, (c) $NaYF_4$–$NaGdF_4$, (d) $NaYF_4$–$NaTmF_4$, (e) $NaYF_4$–$NaYbF_4$, and (f) $NaYF_4$–$NaLuF_4$. Scale bar = 10 nm (a–d) and 20 nm (e,f). The HR-HAADF images clearly show the core–shell structures with compressively strained epitaxial growth (a-c) with high beam stability, while under identical conditions, all the tensile strained epitaxial core–shell structures (d–f) undergo rapid beam damage (see Supporting Information Figures S12–S17 for different magnifications).

resulting in SK layer-island growth. Also, the presence of small nanocrystals (Figure 2d and Supporting Information Figure S29) from the shell precursors clearly demonstrates the reaction-limited nature of the epitaxial growth. Moreover, because of the reaction-limited growth, the SNCs, which are cubic phase, rather than depositing on the hexagonal phase core after dissolution, have separately nucleated and grown as hexagonal phase nanocrystals as confirmed from the HAADF image (Supporting Information Figure S14). This is further supported by the fact that the XRD pattern of the core–shell structure does not have

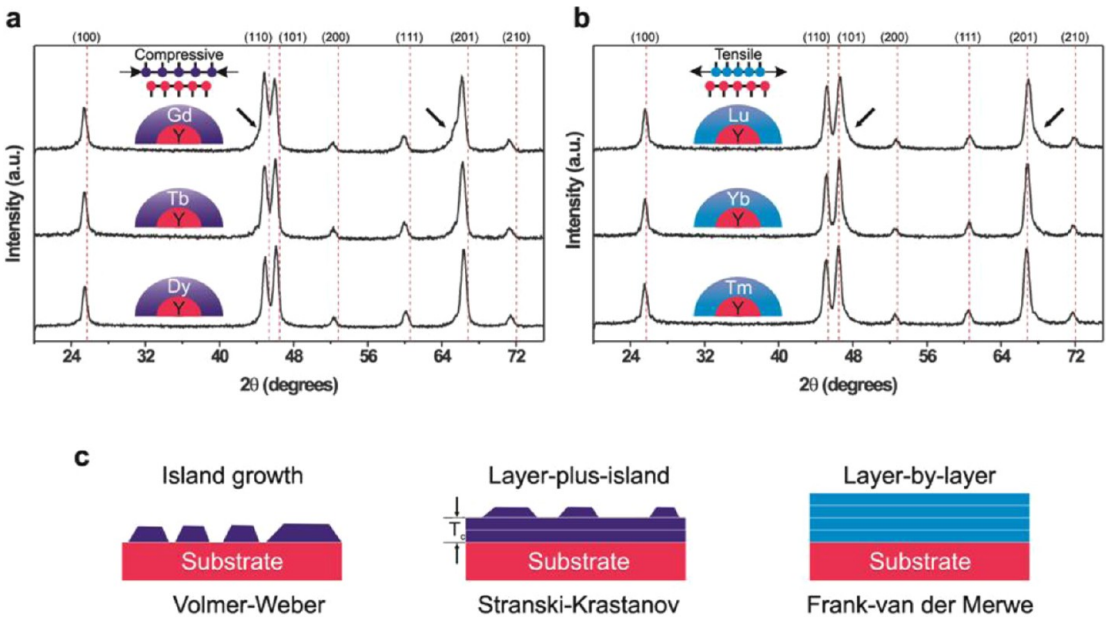

Figure 8. XRD patterns and epitaxial growth modes. XRD patterns of core−shell nanocrystals with (a) compressed shell and (b) tensile shell. Red vertical lines correspond to the hexagonal phase $NaYF_4$ (JCPDS 016-0334) core diffraction pattern. The diffraction peaks of the core−shell structures with compressively strained shell (a) are shifted to lower diffraction angles relative to the core diffraction pattern, while the structures with tensile strained shell (b) match with the core lattice pattern (see also Supporting Information Figures S24 and S25), demonstrating the coherent epitaxial growth in the case of tensile strained epitaxial growth. The diffraction peaks are also observed to be nonsymmetrical and slightly broadened toward lower diffraction angles for a compressively strained shell (a) and to higher diffraction angles for a tensile strained shell (b) (highlighted with black arrows). (c) Schematic representation of different epitaxial growth modes. Volmer−Weber growth results only in island formation, whereas Stranski−Krastanov (SK) growth is layered growth for a few MLs (T_c, critical thickness) that transforms to island growth with increasing thickness. On the other hand, Frank−van der Merwe growth is layer-by-layer growth that is conformal and coherent to the substrate.

any cubic phase features (Supporting Information Figure S24). TEM images of the compressively strained epitaxial core−shell structures with magnitude of lattice mismatch almost identical to that in $NaYF_4$−$NaGdF_4$ also show the presence of smaller nanocrystals (Supporting Information Figures S8b, S9a, and S10a), confirming the generality of our observations. For the tensile shell growth, the conformal and coherent nature of the epitaxial layer even after ~9 MLs establishes that they follow the Frank−van der Merwe layer-by-layer growth mode. Conventionally, the transformation in growth mode during heteroepitaxial growth is considered to be driven by the magnitude of lattice mismatch.[3] However, here we show that the growth mode differs simply upon reversing the sign of lattice mismatch, resulting from the anharmonicity of the interatomic interactions. Thus, heteroepitaxial conformal and coherent shell growth on a given lanthanide core nanocrystal is favored only when the shell lattice parameter is smaller than the core.

On the basis of the findings reported here using lanthanide-based heterostructures, we discuss possible implications for the understanding of epitaxial growth in other nanoscale heterostructures. The universality of only the minimal mismatch consideration to grow conformal core−shell structures is debatable, considering that conformal core−shell structures with much larger lattice mismatch (>5%) have been demonstrated.[17−19] Moreover, under identical magnitude of lattice mismatch, heterostructures with completely different structural morphology are also observed; for example, Pt−Au (4%) results in anisotropic structures,[3] while CdSe−CdS (4%) epitaxial growth is conformal.[20,21] Our experimental results allow for rationally explaining the structural difference between CdSe−CdS (conformal) and Pt−Au (nonconformal) heterostructures with identical magnitude of mismatch (4%), as the former is tensile strained while the latter is compressively strained epitaxial growth. In addition, conformal heteroepitaxial core−shell structures reported with larger magnitude of lattice mismatch (>5%) all have a tensile strained shell.[17−19] Furthermore, our findings provide unique insight on the heteroepitaxial growth of any two lattice mismatched structures (A-B) and its inverted structure (B-A), where one is tensile and the other compressively strained epitaxial growth. Based on our experimental evidence, only the tensile strained structure will be conformal and coherent, while the inverted compressively strained structure will not have the same structural morphology.[22,23] Most importantly, there is no reported evidence of conformal core−shell structures with identical inverted structures nor any conformal and coherent (colloidal) core−shell structure with a compressively strained epitaxial layer (above 1−2 MLs),

which can be attributed to the compressive and tensile asymmetry in epitaxial growth observed here. This in fact suggests that our findings have a much wider implication than just for lanthanide-based systems. The experimental findings reported here are unique and significant considering that such studies even in well-established epitaxial growth on single crystal flat substrates with sophisticated deposition techniques have relied mostly on theoretical investigations.[23−26] Indeed, our experimental results validate those theoretical predictions, and importantly, we show that the influence of sign of lattice mismatch observed in single crystal flat substrates is also applicable in multifaceted zero-dimensional (0D) colloidal nanostructures.

CONCLUSIONS

In summary, we have demonstrated the critical role and the necessity of including the sign of lattice mismatch in designing heteroepitaxial lanthanide-based core−shell nanostructures, as conformal and coherent epitaxial shell growth (above 1−2 MLs) is only possible with a tensile strained shell. The fundamental anharmonicity of the interatomic interactions leads to this striking difference in epitaxial growth of compressed and tensile strained shell and is thus expected to be general for any lattice mismatched epitaxial heterostructure growth. Moreover, our general conclusions will also be valid for (heavily) doped $NaLnF_4$ nanostructures because the unit cell will shrink/expand proportionally for solid solution of $NaLn(1)F_4$ and $NaLn(2)F_4$[27] and probably also holds for doped $LiLnF_4$, $KLnF_4$, and LnF_3 systems. Given the wide ranging applicability of core−shell structures, for example, in tailoring the optical properties of lanthanide-based nanostructures,[7−10,28−30] our study provides a fundamental insight toward precisely tailoring heteroepitaxial growth and should have important implications in various applications of nanoscale materials.

MATERIALS AND METHODS

Chemicals. Yttrium(III) acetate hydrate (99.9%), erbium(III) acetate hydrate (99.9%), dysprosium(III) chloride hexahydrate (99.99+%), lutetium(III) oxide (99.9%), ytterbium(III) oxide (99.99%), thulium(III) oxide (99.9%), dysprosium(III) oxide (99.9%), terbium(III) oxide (99.99%), gadolinium(III) oxide (99.99+%), europium(III) oxide (99.99%), samarium(III) oxide (99.99%), sodium trifluoroacetate (98%), ammonium fluoride (99.99+%), tech grade oleic acid (90%), tech grade 1-octadecene (90%), and hexanes were purchased from Sigma-Aldrich. Oleylamine (97%) from Acros, anhydrous ethanol from Commercial Alcohols, and methanol from Caledon were used. All chemicals were used as received.

Synthesis of Core Nanocrystals. *Synthesis of Hexagonal Phase (β) $NaYF_4$ Nanocrystals.* The synthesis was adapted from a reported procedure, with slight modifications.[13] $Y(CH_3CO_2)_3 \cdot xH_2O$ (1.0 mmol) was added to a 100 mL flask containing oleic acid (6 mL) and 1-octadecene (15 mL) and heated to 125 °C under vacuum for 45 min and cooled to room temperature. To this solution at room temperature was added dropwise a methanol solution (10 mL) of ammonium fluoride (4 mmol) and sodium hydroxide (2.5 mmol) that was stirred for 30 min. The reaction mixture was then heated to 70 °C to remove methanol and subsequently heated to 300 °C (∼10 °C/min) under argon and maintained for 60 min to obtain the core nanocrystals.

Synthesis of Hexagonal Phase (β) $NaErF_4$ Nanocrystals. The synthesis was carried out exactly as outlined for hexagonal (β) $NaYF_4$ NCs mentioned above, except that $Er(CH_3CO_2)_3 \cdot xH_2O$ (1.0 mmol) and oleic acid (4.5 mL) were used.

Synthesis of Hexagonal Phase (β) $NaDyF_4$ Nanocrystals. $DyCl_3 \cdot 6H_2O$ (1.0 mmol) was added to a 50 mL flask containing oleic acid (2 mL) and 1-octadecene (12 mL) and heated to 140 °C under vacuum for 60 min and cooled to room temperature. To this solution at room temperature was added dropwise a methanol solution (7 mL) of ammonium fluoride (4 mmol) and sodium hydroxide (2.5 mmol) that was stirred for 30 min. The reaction mixture was then heated to 70 °C to remove methanol and subsequently heated to 300 °C (∼10 °C/min) under argon and maintained for 60 min to obtain the core nanocrystals.

Synthesis of Sacrificial Nanocrystals (SNCs). *Synthesis of Cubic Phase (α) $NaLnF_4$ (Ln: Sm, Eu, Gd, Tb, Dy, Tm, Yb, Lu) Nanocrystals.* Cubic $NaLnF_4$ NCs were synthesized based on a previously reported procedure with slight modifications.[11] In a typical synthesis, Ln_2O_3 (Ln: Sm, Eu, Gd, Tb, Dy, Tm, Yb, Lu) (1 mmol) was mixed with 10 mL of 50% aqueous trifluoroacetic acid and refluxed at 90 °C overnight (*except for Ln: Tm, Yb, Lu, 25 mL of 50% aqueous trifluoroacetic acid was used and refluxed at 90 °C for 24 h, or until a clear solution was obtained*). The trifluoroacetate precursor ($Ln(CF_3COO)_3$) was obtained after removing excess trifluoroacetic acid and water by evaporation at 65 °C. Sodium trifluoroacetate (2 mmol) was added to the precursor along with oleic acid (6 mL), oleylamine (6 mL), and 1-octadecene (12 mL) and heated to 120 °C under vacuum for 45 min to remove residual water and oxygen. The obtained transparent solution was subsequently heated to 290−295 °C (∼20 °C/min) under argon and vigorously stirred until the reaction mixture turned turbid. Once turbid, the reaction was left for another 5 min and then cooled to room temperature. The NCs were precipitated by adding ethanol (25 mL), collected by centrifugation (1800*g*), washed with ethanol (30 mL), and finally dispersed in hexane (10 mL).

For the shell growth, calculated amount of SNCs were injected (*see following section*). Before injection, the synthesized SNCs dispersed in hexane were taken and a measured volume of the dispersion (200 μL) was transferred to a preweighed vial, and hexane was removed by bubbling with argon. The SNCs in the vial were dried overnight at 70 °C under vacuum, and the vial was then weighed to determine the total organic and inorganic content (ligand and SNCs). The percentage of organic ligands was then determined by thermogravimetric analysis (TGA) and subtracted to obtain the total inorganic content in a given volume and the crystal yield. The SNCs were then aliquoted into vials such that each contained 0.5 mmol of inorganic content.

Synthesis of Core−Shell Nanocrystals. The synthesis was adapted from our previously reported procedure based on self-focusing by Ostwald ripening.[15] All the core−shell nanocrystals were synthesized following exactly the same reaction conditions described below, irrespective of the core−shell composition. The core NCs were synthesized as described above, and after 60 min at 300 °C when the core NCs had formed, about 1 mL of the reaction mixture was retrieved (core) and immediately a calculated amount (0.5 mmol) of sacrificial NCs (SNCs) (α-$NaLnF_4$, Ln: Sm, Gd, Tb, Dy, Tm, Yb, Lu) in 1 mL of octadecene was injected (*for injection, the aliquoted 0.5 mmol of hexane dispersion of SNCs was taken and mixed with 1 mL of octadecene followed by bubbling argon to remove the hexanes*) and ripened for 10 min, followed by two more SNC injections (0.5 mmol each) and ripening cycle of 10 min each to yield core−shell NCs. After the third injection and ripening cycle (total SNCs deposited 1.5 mmol), the reaction mixture was then cooled to room temperature and the core−shell NCs were precipitated by

adding ethanol (20 mL), collected by centrifugation (1800*g*), and washed with ethanol (30 mL) before dispersing them in hexane (10 mL).

Characterization. Transmission electron microscopy images were obtained from a JEOL JEM-1400 microscope operating at 80 kV. Hexane dispersions of the NCs were drop-cast on a Formvar carbon-coated grid (300 mesh Cu) and air-dried before imaging. Size analysis of NCs from the images was obtained by measuring at least 100 particles and averaged. X-ray diffraction patterns with a resolution of 0.05° (2θ) and a scan speed of 1°/min were collected using a Rigaku Miniflex diffractometer with a Cr source (Kα radiation, $\lambda = 2.2890$ Å) operating at 30 kV and 15 mA. Thermogravimetric analysis was done using TA Instruments (SDT Q600), and the weight loss was analyzed by heating from room temperature to 600 °C at the rate of 10 °C/min. High-angle annular dark-field images were acquired on a FEI Titan high base microscope (FEI company, Eindhoven, The Netherlands) operated at 200 kV, equipped with a Gatan Tridiem ER energy filter (GIF) (Gatan Inc., Pleasanton, CA), CEOS image corrector, and a CEOS probe corrector. The STEM detector acceptance angle was 64–200 mrad, convergence angle was 19 mrad, and the GIF collection angle was 22 mrad. Spectrum image acquisition and postprocessing was done using the Gatan Digital Micrograph Software. STEM micrograph collection was performed using the FEI TIA software. Nanoparticles in hexane were deposited directly onto an ultrathin holey carbon support film grid (Ted Pella, Inc., Redding, CA). The samples were plasma cleaned in a Gatan Solaris 950 plasma cleaner twice for 30 s at 50 W to remove hydrocarbon contaminations. Cryo-TEM was obtained using a Gatan 613 cryo-holder at liquid nitrogen temperature and imaged at 200 and 80 kV.

Conflict of Interest: The authors declare no competing financial interest.

Acknowledgment. This work was supported by the Natural Science and Engineering Research Council (NSERC), the Canada Foundation for Innovation (CFI), and the British Columbia Knowledge Development Fund (BCKDF). The authors thank A. Korinek at the Canadian Centre for Electron Microscopy (McMaster University) supported by NSERC and other government agencies for HAADF imaging.

Supporting Information Available: Complete details of characterization using TEM, HAADF, and XRD are provided in the Supporting Information. This material is available free of charge *via* the Internet at http://pubs.acs.org.

REFERENCES AND NOTES

1. Zhang, J. T.; Tang, Y.; Lee, K.; Min, O. Y. Nonepitaxial Growth of Hybrid Core–Shell Nanostructures with Large Lattice Mismatches. *Science* **2010**, *327*, 1634–1638.
2. Carbone, L.; Cozzoli, P. D. Colloidal Heterostructured Nanocrystals: Synthesis and Growth Mechanisms. *Nano Today* **2010**, *5*, 449–493.
3. Habas, S. E.; Lee, H.; Radmilovic, V.; Somorjai, G. A.; Yang, P. Shaping Binary Metal Nanocrystals through Epitaxial Seeded Growth. *Nat. Mater.* **2007**, *6*, 692–697.
4. Abel, K. A.; Boyer, J. C.; Andrei, C. M.; van Veggel, F. C. J. M. Analysis of the Shell Thickness Distribution on $NaYF_4$/$NaGdF_4$ Core/Shell Nanocrystals by EELS and EDS. *J. Phys. Chem. Lett.* **2011**, *2*, 185–189.
5. Zhang, C.; Lee, J. Y. Prevalence of Anisotropic Shell Growth in Rare Earth Core–Shell Upconversion Nanocrystals. *ACS Nano* **2013**, *7*, 4393–4402.
6. Johnson, N. J. J.; van Veggel, F. C. J. M. Sodium Lanthanide Fluoride Core–Shell Nanocrystals: A General Perspective on Epitaxial Shell Growth. *Nano Res.* **2013**, *6*, 547–561.
7. Wang, F.; Deng, R.; Wang, J.; Wang, Q.; Han, Y.; Zhu, H.; Chen, X.; Liu, X. Tuning Upconversion through Energy Migration in Core–Shell Nanoparticles. *Nat. Mater.* **2011**, *10*, 968–973.
8. Zhang, F.; Che, R.; Li, X.; Yao, C.; Yang, J.; Shen, D.; Hu, P.; Li, W.; Zhao, D. Direct Imaging the Upconversion Nanocrystal Core/Shell Structure at the Subnanometer Level: Shell Thickness Dependence in Upconverting Optical Properties. *Nano Lett.* **2012**, *12*, 2852–2858.
9. Huang, P.; Zheng, W.; Zhou, S.; Tu, D.; Chen, Z.; Zhu, H.; Li, R.; Ma, E.; Huang, M.; Chen, X. Lanthanide-Doped $LiLuF_4$ Upconversion Nanoprobes for the Detection of Disease Biomarkers. *Angew. Chem., Int. Ed.* **2014**, *53*, 1252–1257.
10. Wen, H.; Zhu, H.; Chen, X.; Hung, T. F.; Wang, B.; Zhu, G.; Yu, S. F.; Wang, F. Upconverting Near-Infrared Light through Energy Management in Core–Shell–Shell Nanoparticles. *Angew. Chem., Int. Ed.* **2013**, *52*, 13419–13423.
11. Mai, H. X.; Zhang, Y. W.; Si, R.; Yan, Z. G.; Sun, L. D.; You, L. P.; Yan, C. H. High-Quality Sodium Rare-Earth Fluoride Nanocrystals: Controlled Synthesis and Optical Properties. *J. Am. Chem. Soc.* **2006**, *128*, 6426–6436.
12. Wang, F.; Han, Y.; Lim, C. S.; Lu, Y. H.; Wang, J.; Xu, J.; Chen, H. Y.; Zhang, C.; Hong, M. H.; Liu, X. G. Simultaneous Phase and Size Control of Upconversion Nanocrystals through Lanthanide Doping. *Nature* **2010**, *463*, 1061–1065.
13. Li, Z. Q.; Zhang, Y.; Jiang, S. Multicolor Core/Shell-Structured Upconversion Fluorescent Nanoparticles. *Adv. Mater.* **2008**, *20*, 4765–4769.
14. Ye, X.; Collins, J. E.; Kang, Y.; Chen, J.; Chen, D. T. N.; Yodh, A. G.; Murray, C. B. Morphologically Controlled Synthesis of Colloidal Upconversion Nanophosphors and Their Shape-Directed Self-Assembly. *Proc. Natl. Acad. Sci. U.S.A.* **2010**, *107*, 22430–22435.
15. Johnson, N. J. J.; Korinek, A.; Dong, C.; van Veggel, F. C. J. M. Self-Focusing by Ostwald Ripening: A Strategy for Layer-by-Layer Epitaxial Growth on Upconverting Nanocrystals. *J. Am. Chem. Soc.* **2012**, *134*, 11068–11071.
16. Gao, H. J. Some General Properties of Stress-Driven Surface Evolution in a Heteroepitaxial Thin Film Structure. *J. Mech. Phys. Solids* **1994**, *42*, 741–772.
17. Smith, A. M.; Mohs, A. M.; Nie, S. Tuning the Optical and Electronic Properties of Colloidal Nanocrystals by Lattice Strain. *Nat. Nanotechnol.* **2009**, *4*, 56–63.
18. Jin, M.; Zhang, H.; Wang, J.; Zhong, X.; Lu, N.; Li, Z.; Xie, Z.; Kim, M. J.; Xia, Y. Copper Can Still Be Epitaxially Deposited on Palladium Nanocrystals To Generate Core–Shell Nanocubes Despite Their Large Lattice Mismatch. *ACS Nano* **2012**, *6*, 2566–2573.
19. Tsuji, M.; Yamaguchi, D.; Matsunaga, M.; Ikedo, K. Epitaxial Growth of Au@Ni Core–Shell Nanocrystals Prepared Using a Two-Step Reduction Method. *Cryst. Growth Des.* **2011**, *11*, 1995–2005.
20. Peng, X. G.; Schlamp, M. C.; Kadavanich, A. V.; Alivisatos, A. P. Epitaxial Growth of Highly Luminescent CdSe/CdS Core/Shell Nanocrystals with Photostability and Electronic Accessibility. *J. Am. Chem. Soc.* **1997**, *119*, 7019–7029.
21. Chen, O.; Zhao, J.; Chauhan, V. P.; Cui, J.; Wong, C.; Harris, D. K.; Wei, H.; Han, H. S.; Fukumura, D.; Jain, R. K.; *et al.* Compact High-Quality CdSe–CdS Core–Shell Nanocrystals with Narrow Emission Linewidths and Suppressed Blinking. *Nat. Mater.* **2013**, *12*, 445–451.
22. Sanchez, S. I.; Small, M. W.; Zuo, J. M.; Nuzzo, R. G. Structural Characterization of Pt–Pd and Pd–Pt Core–Shell Nanoclusters at Atomic Resolution. *J. Am. Chem. Soc.* **2009**, *131*, 8683–8689.
23. Lu, Y.; Przybylski, M.; Trushin, O.; Wang, W. H.; Barthel, J.; Granato, E.; Ying, S. C.; Ala-Nissila, T. Strain Relief in Cu–Pd Heteroepitaxy. *Phys. Rev. Lett.* **2005**, *94*, 146105.
24. Hsiao, P. Y.; Tsai, Z. H.; Huang, J. H.; Yu, G. P. Strong Asymmetric Effect of Lattice Mismatch on Epilayer Structure in Thin-Film Deposition. *Phys. Rev. B* **2009**, *79*, 155414.
25. Trushin, O.; Granato, E.; Ying, S. C.; Salo, P.; Ala-Nissila, T. Minimum Energy Paths for Dislocation Nucleation in Strained Epitaxial Layers. *Phys. Rev. B* **2002**, *65*, 241408.
26. Trushin, O.; Granato, E.; Ying, S. C.; Salo, P.; Ala-Nissila, T. Energetics and Atomic Mechanisms of Dislocation Nucleation in Strained Epitaxial Layers. *Phys. Rev. B* **2003**, *68*, 155413.
27. Sudarsan, V.; van Veggel, F. C. J. M.; Herring, R. A.; Raudsepp, M. Surface Eu^{3+} Ions Are Different than "Bulk" Eu^{3+} Ions in Crystalline Doped LaF_3 Nanoparticles. *J. Mater. Chem.* **2005**, *15*, 1332–1342.

28. Li, X.; Wang, R.; Zhang, F.; Zhao, D. Engineering Homogeneous Doping in Single Nanoparticle To Enhance Upconversion Efficiency. *Nano Lett.* **2014**, *14*, 3634–3639.
29. Liu, Y.; Tu, D.; Zhu, H.; Li, R.; Luo, W.; Chen, X. A Strategy To Achieve Efficient Dual-Mode Luminescence of Eu^{3+} in Lanthanides Doped Multifunctional $NaGdF_4$ Nanocrystals. *Adv. Mater.* **2010**, *22*, 3266–3271.
30. Chen, G.; Ohulchanskyy, T. Y.; Liu, S.; Law, W.-C.; Wu, F.; Swihart, M. T.; Agren, H.; Prasad, P. N. Core/Shell $NaGdF_4$:Nd^{3+}/$NaGdF_4$ Nanocrystals with Efficient Near-Infrared to Near-Infrared Downconversion Photoluminescence for Bioimaging Applications. *ACS Nano* **2012**, *6*, 2969–2977.